ELSEVIER

Journal of Power Sources 105 (2002) 169–181

JOURNAL OF POWER SOURCES

www.elsevier.com/locate/jpowsour

Power limitations of supercapacitor operation associated with resistance and capacitance distribution in porous electrode devices

B.E. Conway*, W.G. Pell

Chemistry Department, Faculty of Science, University of Ottawa, 10 Marie Curie Street, Ottawa, Ont., Canada K1N 6N5

Abstract

By analogy with the behavior of vacuum (air) capacitors, early perceptions of the properties of electrochemical supercapacitors were that very high power-levels would be achievable because only capacitance (ca. 25 μF cm^{-2}) originating from a double-layer of nanometre thickness was involved. However, for device applications, the required large capacitances (0.50 F g^{-1}) are achievable only by use of high-area porous-*C* matrices (ca. 1 to 2×10^3 m^2 g^1). Then the capacitance is only accessible through a complex series/parallel distribution of reduced current (RC) networks leading to a *power-spectrum* in which only a fraction of expected charge is accessible at high rates. The equivalent circuit then approximates to that of a transmission-line. Characterization of power limitation effects is demonstrated by results of experiments on porous-*C* electrodes by means of linear-sweep voltammetry, complementary dc charge/discharge curves and by real-time simulations of the behavior of a 5-element hardware RC circuit. The distribution of *R* and *C* elements in a porous electrode structure leads to a decline of energy-density with operating power-density as current drain is increased. It is shown how this can be represented by Ragone plots for capacitors, taking account of declining voltage with state of discharge. Practical comparisons are made with the behavior of three, non-aqueous capacitor modules.

Keywords: Porous electrodes; Electrochemical capacitors; Cyclic voltammetry; Ragone relations

1. Introduction

Amongst the projected applications of supercapacitors as energy storage and delivery devices, complementary to batteries, are their use as high-power systems for load-leveling in hybrid arrangements with batteries or fuel-cells for electric vehicles, or as direct cold-starting energy reservoirs, when charged. Another application requiring high-power, but short duration, electrical-energy pulses is for bridging short-period line power-outages.

In early discussions of the properties of electrochemical supercapacitors, perceptions existed that the simple process of discharging previously charged double-layers in a conjugately configured ± pair could be conducted at very high power-densities. However, this is only the case for an ideal capacitor (Fig. 1a) unimpeded by any real or equivalent resistance in series (ESR) (Fig. 1b). Any real capacitor suffers impedance to high charging or discharging rates on account of real and/or ESR.

In order for electrochemical double-layer capacitor devices to store appreciable and practically significant charge-density and, hence electrical energy density (e.d.), their interfaces have to be established in modules having very high areas, e.g. at porous carbon felts, powders or aerogels or, in the case of pseudocapacitative devices [1–4], at high-area redox-oxide surfaces. Then capacitances on the order of 50–100 F g^{-1} of electrode material can be realized [3,4]. On account of the above and now well known requirement for use of porous electrodes, the double-layer or interfacial redox pseudocapacitance (e.g. as developed at RuO_2 [1,2]) is only accessible through a distributed ohmic resistance of the invading electrolyte and the contact resistances between the carbon matrix or oxide particles. A distributed RC network then arises [5], as in Fig. 1d (through 1c), having a distribution of RC time-constants which restrict the immediately available power (*P*) from the system on discharge, or the reverse on charge. The electrical behavior of the system then corresponds to a power spectrum and the equivalent circuit (Fig. 1d) to that of a transmission-line as treated in a seminal series of papers by de Levie [5,7] and one by Keiser et al. [6]. This situation means that only a fraction of the charge can be withdrawn at high rates, while more is available at low rates, and all under conditions of low dc discharge current or low frequency in ac modulation.

In power delivery systems there is an important and fundamental relation between power-density (p.d.) delivery and achieved operating e.d. This tends to diminish with

* Corresponding author. Tel.: +1-613-562-5481; fax: +1-613-562-5170.

0378-7753/02/$ – see front matter
PII: S0378-7753(01)00936-3

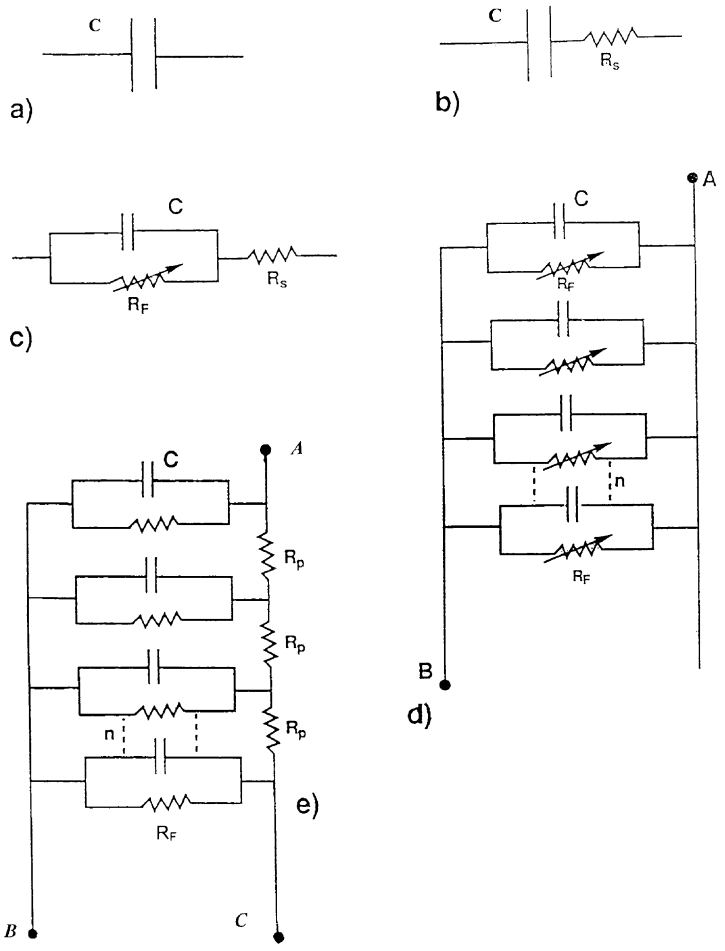

Fig. 1. Hierarchy of equivalent-circuits for capacitor and capacitor network electrical behavior: (a) simple capacitor; (b) capacitor with equivalent or real series resistance; (c) capacitor with series resistance and potential-depended Faradaic leakage resistance, R_F; (d) parallel combination of nC and R_F leakage elements (overall RC constant is $R_F/n \times nC \equiv R_F C$) for the single element; (e) parallel C, R_F elements connected with pore-resistance elements R_p (related to transmission-line, constant phase element, but with R_F lekeage pathways.

increasing p.d. demand. This is a result of fundamental aspects of the thermodynamics of irreversible processes involving dissipative losses. Practically, the dependence of e.d. of an operating power delivery system on p.d. can be usefully represented by so-called Ragone diagrams [4,8] often plotted on log/log axes. For many years, Ragone plots have been used to characterize p.d./e.d. relations for battery performance. Only recently have they been applied to electrochemical capacitor behavior.

The purpose of the present paper is to bring together the results of four complementary directions of our work on evaluation of the effects of porosity, and distribution of interconnected capacitative (C) and ohmic (R) elements, on the electrical charging and discharging behavior of porous electrode electrochemical capacitors, especially the power limitations that those effects introduce into the operating characteristics of such devices, including restrictions to charge admission in high-rate applications. The following aspects are examined: (a) behavior of a model 5-element (cf. [10]) RC hardware circuit; (b) behavior of three, real non-aqueous electrolyte, carbon double-layer capacitors, specially fabricated to demonstrate the role of significant distributed internal resistance; (c) the electrical behavior of de Levie [7] wire-brush electrodes as models for linear pores in a porous electrode module; and (d) the electrical behavior of real double-layer capacitor modules containing sub-optimal concentrations of electrolyte in order to enhance distributed resistance effects and enable them to be better evaluated quantitatively.

2. Experimental

The experimental procedures employed for testing and evaluating the electrical behavior of supercapacitors and porous electrodes used in their construction have been described in a variety of works published elsewhere (e.g. [2–4,9]). Commonly, the following procedures have been employed, as in the present work.

1. Cyclic voltammetry (CV), conducted at various potential (V) sweep-rates s ($\mathrm{V\,s^{-1}}$) with recording of the

potential-, and s-dependent response currents, I, which are related by

$$C = \frac{I}{s} \quad (1)$$

where C is the capacitance of the electrode interface. Since $Cs = I$, this procedure, operated overe a range of $\forall s$ values, corresponds to charging or discharging of C at various rates and thus at various power-levels. In the CV procedure, the electrode is subject to polarization over a range of potentials, $V_1 \rightarrow V_2$, then $V_2 \rightarrow V_1$ in a repetitive manner at constant $\pm s$, depending on the direction of sweep. An ideal capacitor (constant C) then gives a rectangular I versus V response plot for a given $+s$ and $-s$ rate of modulation of V.

2. Constant-current (I) or current-density (i) charging and discharging: then the recorded response variable is the time-dependent potential, V. Then $\int I\,\mathrm{d}t$ over the charge/discharge plots gives the time-, and V-dependent delivery of charge, Q. The power factor is determined by the product $I \times V$ or per cm^2 by $i \times V$, and the e.d. by $Q \times V$ through the charging curve.
3. Impedance spectroscopy conducted over a range of impressed frequencies. Additionally, in the present work, use of a 4-, or 5-element hardware model RC circuit (Fig. 2) at which local polarization potentials and admission or delivery currents could *individually* be recorded in time down the ladder of RC elements under conditions of charge or discharge, or under CV. Of course, within a real porous electrode, sampling of local potentials and currents is not feasible.

In order further to examine the role of internal electrolyte resistance in the behavior of porous capacitor electrodes, we have studied the CV behavior of de Levie [7] brush electrodes made from an assembly of thin Ag or Au wires, 5 cm in length, and constricted within a shrinkable PVC tube into which the desired electrolyte (aq. H_2SO_4 or aq. NaOH) was admitted under vacuum.

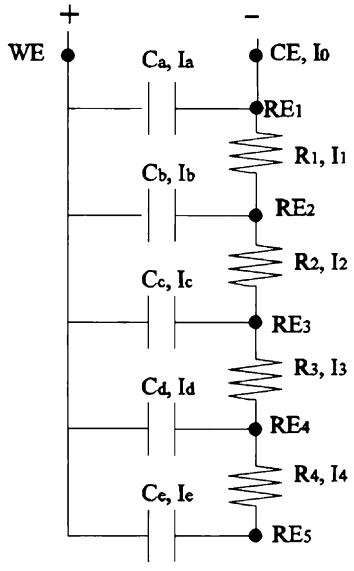

Fig. 2. Series/parallel, 5-element distributed R and C hardware circuit for modeling porous electrode behavior.

Complementarily, three real electrochemical capacitor modules were prepared for us by Redox Engineering Inc. (Winchester, MA) using high-area carbon with an electrolyte of tetrabutylammonium tetrafluoroborate in anhydrous propylene carbonate made up at three concentrations, 1.0, 0.2 and 0.08 M, again to examine performance as a function of internal electrolyte concentration in a "real" system.

3. Results and discussion

3.1. Modeling of porous electrode behavior by means of a five RC-element hardware circuit

The circuit is shown in Fig. 2. Polarization is applied at the "working" (WE) and "counter" (CE) electrodes at the top of the RC ladder. Sampling of response-currents and potentials can be made down the RC ladder in real-time at the connections marked. Cumulative power limitation arises down the ladder network, simulating transmission-line behavior (cf. [5]), owing to the progressive sum of the resistance elements in series-parallel connections to the capacitor (C) elements. Also, delayed dependence of charging down the network arises due to the cumulative series resistance so that "phase difference" arises between current–voltage relations for the inner, compared with the outer, RC elements. Progressive power dissipation also arises down the network of the distributed RC elements and this can be evaluated from charging curves.

The distribution of component charging currents is indicated, in Fig. 2 as I_a, I_b, I_c, I_d, and I_e passing respectively into C_a, C_b, ..., C_e. I_0 is the total charging (or discharging) current admitted between terminals WE and CE, and is equivalent to the sum of the components I_a to I_e. The currents passing respectively through each of $R_1, R_2, \ldots, R_4$, down the "pore", are I_1, I_2, ..., I_4. The five capacitors have capacitance values in the range of 130 to 142 μF and the resistors are approximately 100 kΩ. The values chosen were selected to give conveniently measurable RC relaxation time-constants.

Prior to each experiment, all capacitors in the network were fully discharged (to 0 V), so that the initial open-circuit voltage was 0 V. In each case, 10–15 constant-current charges/discharges of 50, 100 and 200 μA, were applied sequentially between 0 and 9 V across the CE and WE terminals of the network. The recorded voltages were measured between the five "reference" points (RE_1, RE_2, ..., RE_5) corresponding to potential differences V_a to V_e down the hardware circuit (Fig. 2). Cyclic voltammograms were also obtained at various sweep-rates in the usual way using CE also as a reference electrode terminal.

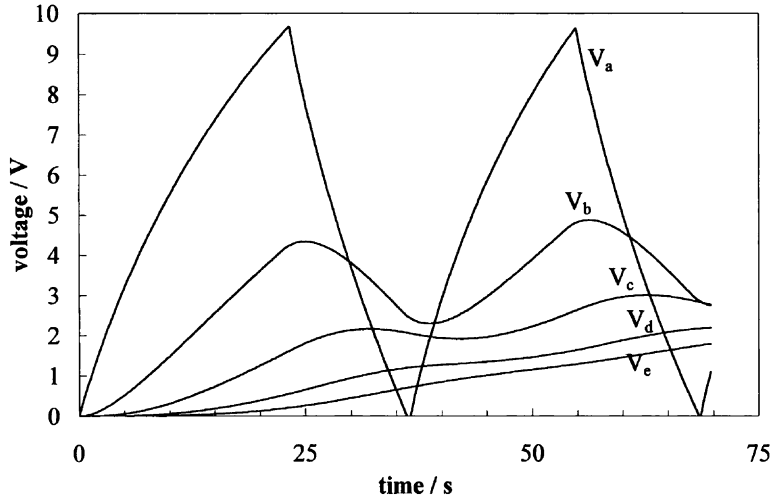

Fig. 3. Voltage vs. time profiles of the first and second cycles addressed to the network, resolved for each of the capacitors shown in Fig. 2, $I_0 = 100$ μA. Curves V_a, V_b, ..., V_e show the separate profiles across each of the five capacitors C_a, C_b, ..., C_e.

3.2. Charge/discharge voltage and current behavior

Fig. 3 shows the 100 μA charge/discharge voltage versus time profiles, and Fig. 4 the corresponding local component current versus time profiles, of the first two cycles addressed to the network. Curves V_a, ..., V_e (and I_a, ..., I_3, respectively) show the separate profiles down the "pore" circuit at the five reference points indicated in Fig. 2. Note the differences of the first and second cycle curves that arise due to the "memory effect" associated with the distribution of charging/discharging times within the complex RC circuit. After the 11th or 12th cycles, a more or less "steady state" in the discharge/recharge processes is reached. Note that attenuation of responses down the "pore" for potentials V_a to V_e and currents I_a to I_e, and the phase-shift between these V and I versus t profiles, is already noticeable in Figs. 3 and 4.

A significant feature of the charging and succeeding discharge curves (Fig. 3), unlike charging/discharging of a regular plane-electrode capacitor, is that they are not linear in time, even for the V_a potential, nor are they mirror-images, thus demonstrating one of the essential features of the electrical behavior of *porous electrode* capacitors. A linear charge/discharge curve is expected for a capacitor (of constant capacitance) charged at constant current. This is not the case for the model RC network, while the total current, I_0, supplied to the network is constant, the current admitted or delivered by each capacitor is not, the result being a voltage response that is non-linear in time (Fig. 3). This distortion becomes characteristically much more significant for the charge/discharge curves further down the "pore", i.e. for potentials V_b, V_c, V_d and V_e as a function of time (Fig. 4), and the differences between first and second cycle charge/discharge curves become much increased as V goes from V_b to V_e (down the pore), with more and more asymmetry.

Interestingly, as I_a is decreasing because of charging of capacitor C_a, I_b, I_c, ..., etc. are *increasing*; corresponding

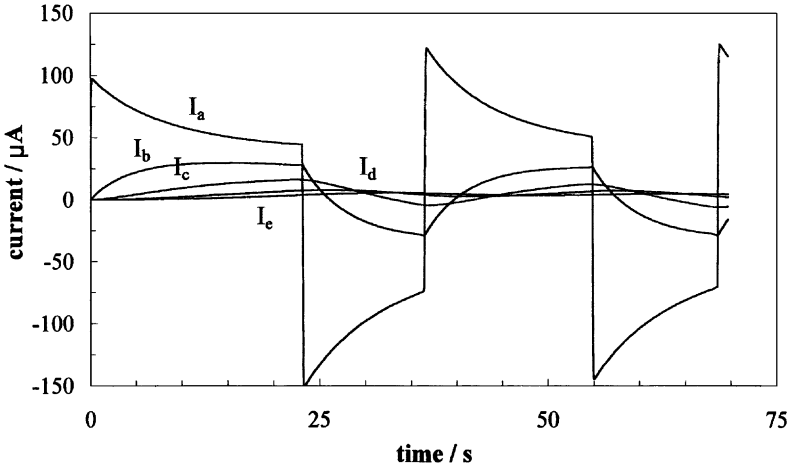

Fig. 4. Current vs. time profiles of the first and second cycles addressed to the network, resolved for each of the capacitors shown in Fig. 1, $I_0 = 100$ μA. Curves I_a, I_b, ..., I_e show the separate profiles of currents passing, respectively, into each of the five capacitors C_a, C_b, ..., C_e.

differences in t-dependence arise in the discharge current profiles. Note that the second cycle profiles are not, respectively, identical to the first cycle ones. However, by the 11th and 12th cycles, it is found that a "steady state" has been set-up and the successive component-current profiles are almost identical in their time-dependence.

Comparison of these figures results in several interesting and significant observations. Firstly, in the early cycles, the current to these inner capacitors is generally positive (i.e. the inner capacitors are continuously being charged even while the outer capacitors discharge). By the 11th and 12th cycles, however, the inner capacitors begin to experience both charge and discharge in the time period required to fully charge and discharge the outermost capacitor, C_a. Secondly, the currents passing to the capacitors after 11 or 12 cycles are smaller than those initially experienced. Thirdly, the shape of the current/time profile changes, especially in the case of I_c (see Fig. 4). With repetition, the current profile becomes more sinusoidal in shape.

3.3. Power, P, and energy, E, losses

We have noted that one of the most significant aspects of the performance of supercapacitors is their perceived capability of delivering power at high power-densities. In addition, the relation of the latter to energy-densities is of corresponding importance, as revealed by Ragone plots [4,8].

From the experimental data for component V and I behavior, it is possible to calculate the power losses, P

$$P_n = [I_n(t)]^2 R_n, \quad \text{for } n = 1, 2, 3, 4 \tag{2}$$

down the circuit ladder. The current components on the first and second cycles, as well as 11th and 12th cycles, down the resistor elements R_1, R_2, ..., R_4 were determined as a function of time.

Power losses on charge/discharge arise on account of energy dissipated across the R elements of the circuit of Fig. 2. Fig. 5 shows the resulting power loss behavior for first and second cycles at 100 μA overall charge/discharge currents giving the component element power losses, P_1, P_2, P_3 and P_4, together with the total P (P_T). Note the unusual shapes of the curves and the difference of the second-cycle component P(time) curves from those for the first cycle. On the 11th and 12th cycles, the component element power P_1 curve is almost identical with the P_T curve while P_2, P_3 and P_4 (≈0) are much smaller for both charge and discharge half-cycles. The differences become exaggerated, because the current components across R elements are squared for the calculation of values of P.

The corresponding energy losses can, of course, also be calculated and are

$$E_n = \int_0^t [I_n(t)]^2 R_n \, dt, \quad \text{for } n = 1, 2, 3, 4 \text{ down the circuit ladder} \tag{3}$$

Fig. 6 shows plots of the component energy losses, E_T, E_1, ..., E_4 versus time for first and second cycles, corresponding to the respective $V(t)$ and $I(t)$ relations shown earlier. The second-cycle behavior is quite different and the energy losses are much diminished. On the 11th and 12th cycles, a "steady-state" response is again almost reached and the two series of curves become almost identical. From the analysis of these integrated resistive losses, the energy storage efficiency, ε, may be calculated. For example, for a 100 μA charge, once "steady state" has been reached, an energy storage efficiency during charge of approximately 85–86% is achieved.

4. The de Levie brush electrode as a model for porous electrode behavior in supercapacitors

In de Levie's classic series of papers [5,7] on porous electrodes, it was shown that a cylindrically constricted

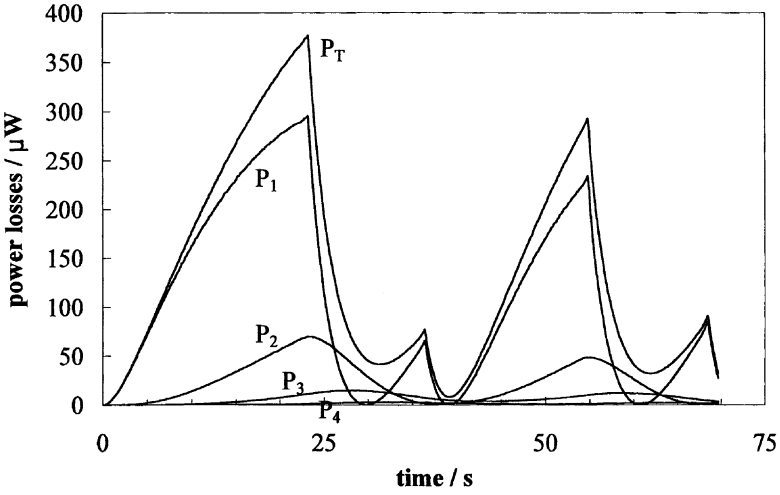

Fig. 5. Component dissipated power losses, P_1, P_2, ..., P_4 through resistors R_1, R_2, ..., R_4, respectively, together with the total power loss, P_T, I_0 = 100 μA; for the first and second cycles.

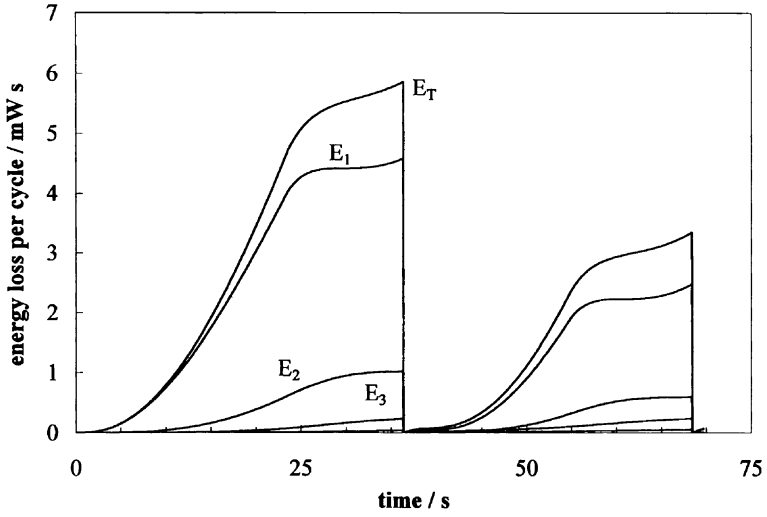

Fig. 6. Component dissipated energy losses per cycle, E_1, E_2, ..., E_4 through resistors R_1, R_2, ..., R_4, respectively, together with the total power loss, E_T, $I_0 = 100$ μA; for the first and second cycles.

packet of parallel thin wires provided a good model for the behavior of a porous electrode, albeit that the resulting pores are linear and anticylindrical in cross-section. In particular, it was shown that the impedance spectrum became like that of a transmission-line exhibiting a -45° phase-angle over a wide range of frequencies.

Earlier, we noted the common application of CV for study of supercapacitor devices. Here we have studied the CV current-response behavior of two de Levie type brush electrodes, one made from thin Ag and a second from thin Au wires. Both these metals exhibit almost potential-independent double-layer capacitance over appreciable ranges of polarization voltage, greater for Au than Ag. Comparatively, the range of almost ideal polarizability at C is ca. 1 V in aqueous media, depending on the source of the C [4].

At increasing sweep-rates, current responses become proportionally larger, ideally according to Eq. (1), this situation corresponding to charge/discharge operation at increasing power-levels (formally, note that the integral $\int i\,\mathrm{d}V(t)$ of the voltammogram, plotted on the $V(t)$ axis is the power involved in the process. At constant s, it scales with the charge $\int i\,\mathrm{d}t$, where $\mathrm{d}t \equiv \mathrm{d}V(t)/s$). However, in the brush electrode geometry, the electrolyte resistance increases down the linear pores with progressive loss of charging/discharging access, as with the hardware model circuit. Resulting dissipative losses can be directly observed in CV measurements, as shown below.

Thus it is to be expected that the measured double-layer capacitance of a porous electrode (and also of a brush electrode) determined from CV studies would show a dependence on sweep-rate. This is due to the fact that at high rates, the measured capacitance simply approaches that of the pore orifice, and it is only as the sweep-rate slows that the signal can "penetrate" (cf. [5]) into the pore, thus giving rise to increased charge acceptance and hence measured

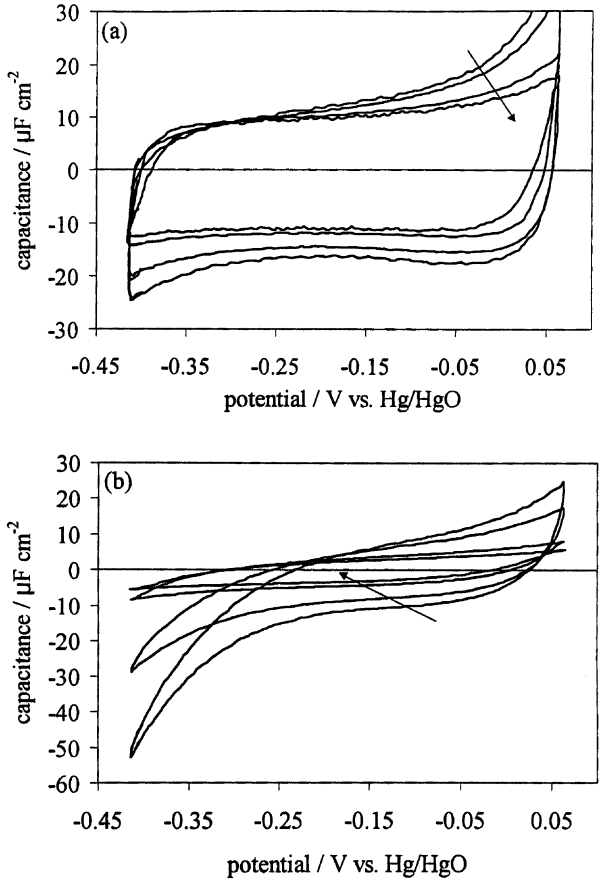

Fig. 7. Cyclic voltammograms expressed as capacitance (I/s) vs. potential between -0.42 and 0.04 V vs. Hg/HgO at 1 V s^{-1} in 0.1 M KOH for (a) silver wire electrode, at sweep-rates 50, 100, 500, and 1000 mV s^{-1}; and (b) a silver brush electrode, at sweep-rates 50, 100, 500, and 1000 mV s^{-1} in (1) 0.02 M H_2SO_4; (2) 0.2 M H_2SO_4; (3) 2.0 M H_2SO_4; arrows indicate direction of increasing sweep-rate. Insert in (3) is CV for single gold wire electrode at 50, 100 and 200 mV s^{-1}.

capacitance. Furthermore, the capacitance versus potential relation in CV will also deviate from the classical square waveform expected for a pure capacitor, due to resistance effects down the pore, as illustrated in the observed behavior of the hardware model circuit.

Results of experiments on the Ag (in 0.1 M aq. KOH) and Au (in 0.02, 0.2 and 2.0 M aq. H_2SO_4) brush electrodes conducted over a range of increasing sweep-rates, s, are shown in Figs. 7 and 8. The response current diagrams for the brush electrodes exhibit decreasing measurable capacitance ($C = I/s$, Eq. (1)) with increase of s (indicated by the direction of the arrows) and deviation from the expected and known, almost "rectangular", form of the voltammograms for double-layer capacitance behavior at a Ag or Au wire. For the corresponding free wires of the same respective metals, normal CV responses are observed, as shown in Fig. 9 for currents at Ag normalized between the wire and the brush geometries by division by the different real electrode areas and in the inset of Fig. 8 for Au. Thus, like the change of impedance spectrum for a brush electrode, shown in [7], there is a major change in the CV current-response behavior of Ag or Au wires when they

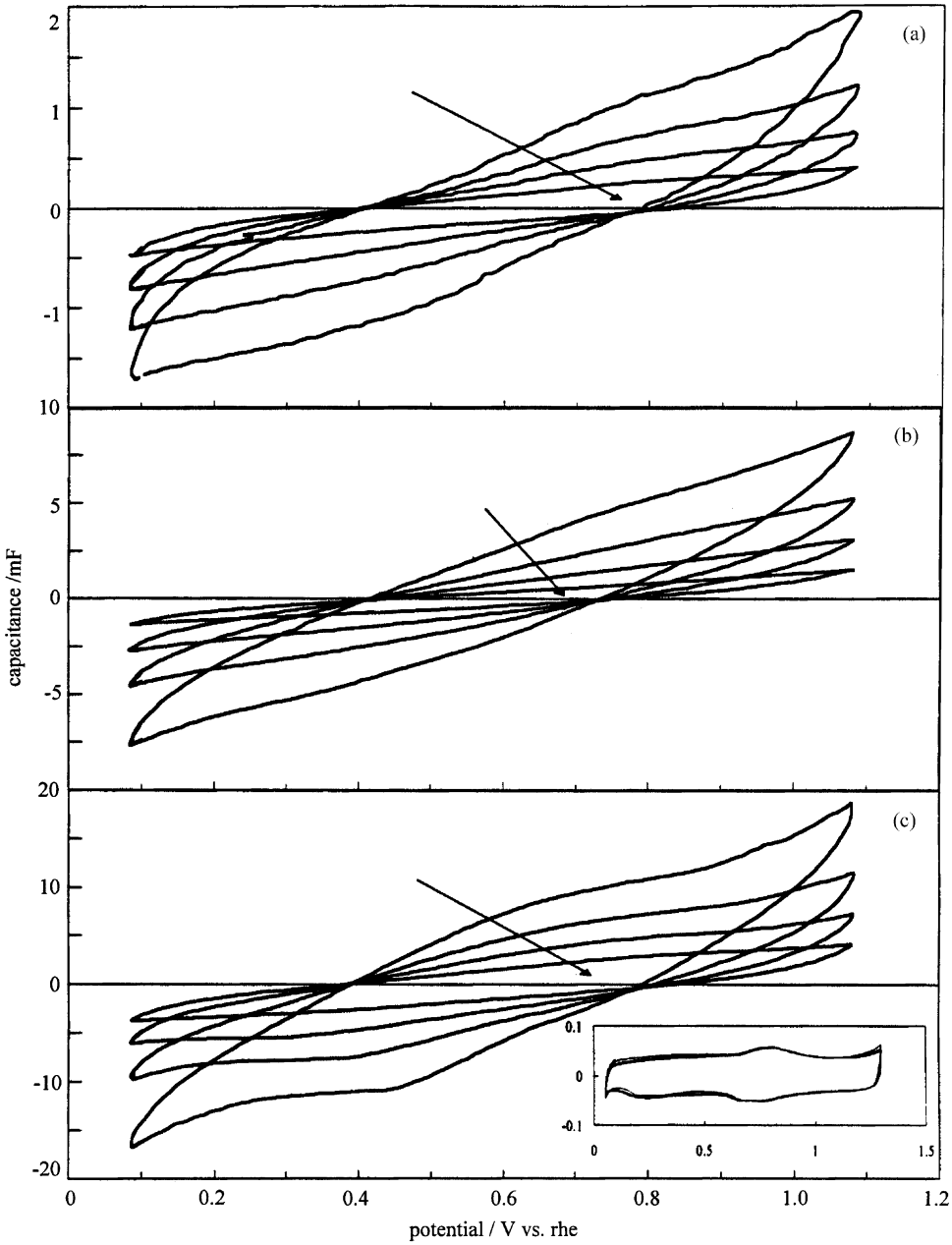

Fig. 8. Cyclic voltammograms for a Au brush electrode expressed as capacitance (I/s) vs. potential between 0 and 1.1 V vs. rhe for sweep-rates 50, 100, 500 and 1000 mV s^{-1} in (a) 0.02 M H_2SO_4; (b) 0.2 M H_2SO_4; (c) 2.0 M H_2SO_4; arrows indicate direction of increasing sweep-rate. Inset in (c) is CV for single gold wire electrode at 50, 100 and 200 mV s^{-1}.

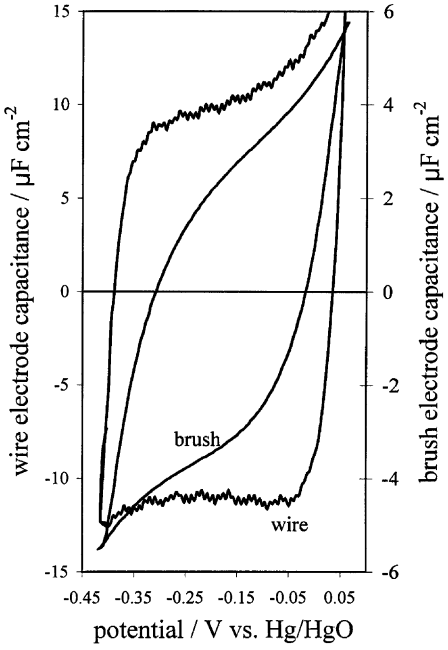

Fig. 9. Cyclic voltammograms expressed as capacitance (I/s) vs. potential between −0.42 and 0.04 V vs. Hg/HgO at 1 V s^{-1} in 0.1 M KOH for silver wire and silver brush electrodes, normalized to the same interfacial area.

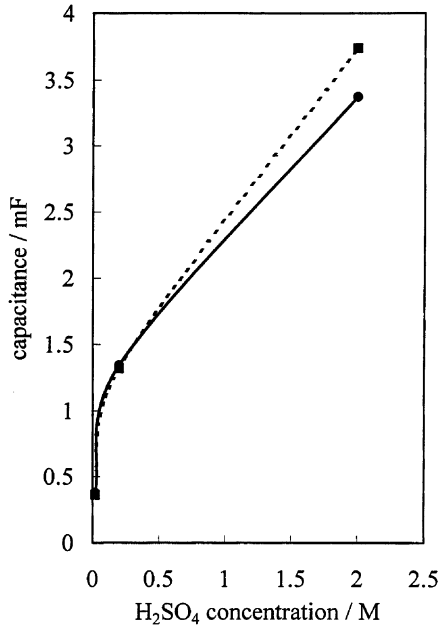

Fig. 10. Capacitance of Au brush electrode as determined from CV curves in Fig. 6 as a function of electrolyte concentration and thus solution resistivity: (- - -) 0.2 V; (—) 1.0 V.

are constrained together in a linear brush configuration, with resulting charging energy and power losses upon potential cycling.

Experiments with the Au brush electrode were conducted at three, diminishing, electrolyte concentrations: 2.0, 0.2 and 0.02 M (Fig. 8). Characteristically, at the brush electrode, in comparison with the free wire one of the same metal, the voltammograms becomes distorted (Figs. 7 and 8) with increasing sweep-rate from the normal, almost rectangular, current-response profile, and with increasing dilution of the electrolyte; the latter leads, of course, to increasing internal distribution of R down the pores of the brush. Correspondingly, the accessibility to charging (or discharging) and the resulting measurable capacitance are attenuated both with increasing s (Fig. 10) and with electrolyte dilution (Fig. 10), as found for the Au brush electrode in 0.02, 0.2 and 2.0 M aq. H_2SO_4. Note that the double-layer capacitance profiles for a free Au wire electrode, shown in the inset of Fig. 8, are virtually *independent of s* over the ranges 50, 100–200 mV s^{-1}. The effects observed at the Au brush electrode, and also the Ag one, are therefore entirely due to the internal resistance distribution introduced by the brush geometry.

Interestingly, computer-calculated voltammograms for a capacitance $C = 1$ F, in series with a resistance $R = 5\ \Omega$, show in Fig. 11, for increasing $S = 5$, 10, 20, 50, 100 and 200 mV s^{-1}, show good qualitative agreement with the trend of behavior of the Au brush electrode with increase of s and also with that of the Redox Engineering Inc., non-aqueous, double-layer capacitor modules, discussed in the final section of this paper.

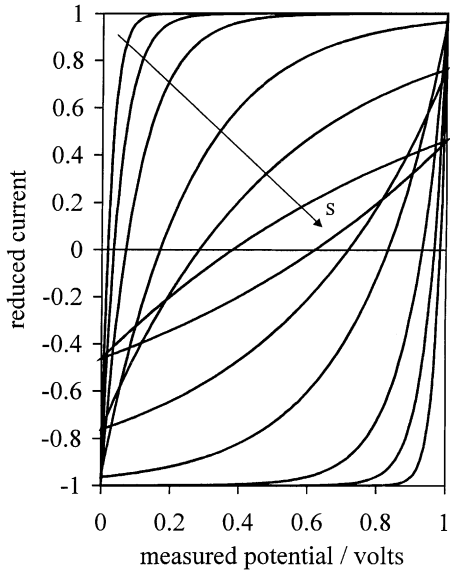

Fig. 11. Calculated cyclic voltammograms for a simple series RC circuit expressed as a function of measured potential ($V_t + IR$) calculated for $R = 5\ \Omega$, $C = 1$ F, range $V_1 = 0$ V, $V_2 = 1$ V; arrow indicates direction of increasing sweep-rate, 5, 10, 20, 50, 100 and 200 mV s^{-1}.

5. Ragone plots for capacitors and batteries

5.1. General basis of Ragone plots

As stated earlier, Ragone plots represent the dependence of achieved energy-densities, E, on operating power-densities, P, the latter being determined by the rates at which charging or discharging of an electrical-energy storage device are conducted.

In a battery, power losses are determined by the combined effects of electrode-kinetic (Tafel relation) and ohmic "*IR*" polarization. Power loss due to the former is dependent on the transcendental product, $I \log I$, while the latter is dependent on I^2R. For an electrochemical capacitor, the situation is importantly different: Tafel polarization is virtually absent, so *IR* losses are dominant but, compared with a number of important battery systems, there is a systematic and intrinsic decline of voltage with diminishing state-of-charge (SOC); hence E and P systematically decline during discharge at constant current, more so than adventitiously arises in the operation of many batteries except the Li–ion intercalation type where quasi-pseudocapacitance is exhibited [2,4]. Additionally, concentration polarization can arise at high rates and/or towards the end of charge in capacitor devices [4].

The relations for power (P) and energy (E) in terms of iR drop and Tafel polarization parameters $\eta_a(i)$, the Tafel polarization slopes, b, for anode and cathode and the respective exchange current-densities, i_0, are

$$\text{Power}\,(P) = i(\Delta V) = i[\Delta V_{\text{rev}} - iR - \Sigma[\eta_a(i)]] \tag{4}$$

$$\text{Power}\,(P) = i\Delta V_{\text{rev}} - i^2R - i\Sigma b \ln i + i\Sigma b \ln i_0 \tag{5}$$

where ΔV_{rev} is the reversible cell voltage at $i = 0$; i, i_0 and $\eta_a(i)$ are related by the Tafel equation.

$$\ln i = \ln i_0 + \frac{\eta_a(i)}{b} \tag{6}$$

Corresponding to Eq. (5) for P, is the equation for the energy E

$$E = Q(\Delta V_{\text{rev}} - iR - \Sigma b \ln i - \Sigma b \ln i_0) \tag{7}$$

in which the terms in the brackets are the same as in Eq. (4) for the current-dependent polarization effect but are multiplied by the stored charge Q instead of by i in Eq. (4).

It is the relation between P in Eq. (5) and E in Eq. (7) that is the basis of Ragone plots for battery systems. For electrical-energy storage by a capacitor the Tafel polarization terms do not normally arise, except with Faradaic pseudocapacitance [3,4,11] at high rates, but, importantly, the operating voltage, ΔV, across the capacitor is dependent on the SOC Q: $\Delta V = Q/C$ and C may also be somewhat dependent on ΔV.

5.2. Ragone plots for electrochemical capacitor behavior

Ragone plots have taken on a new importance in the technology of "hybrid" combination of electrochemical capacitors having high p.d. (but relatively low e.d.) with high e.d. aqueous-electrolyte batteries for electric-vehicle drive trains. For such systems, power-level and energy balancing in the coupling between these two kinds of energy-storage systems is of major importance and consequently requires quantitative knowledge of the Ragone relations for both types of system.

As we show below, the factors that determine the e.d. versus p.d. relations for electrochemical capacitors are significantly different from those for batteries because, on discharge, the *continuous decline* of output voltage is an *intrinsic property* of a charged capacitor (determined by the relation "$C = Q/V$") while, ideally, a battery discharge voltage can remain almost constant (e.g. with $Li/SOCl_2$) so long as the chemical redox species remain in a two-phase electrochemical equilibrium prior to exhaustion of one or other of the reactants.

We now examine how rating of p.d. of a capacitor can be treated and experimentally examined. Because the operating voltage depends on SOC, withdrawal of charge at a rate i causes a corresponding rate of decline in V so that a formal power rating at a particular i depends on the state of discharge of the capacitor.

With the usual definition of p.d. as "iV" we have

$$P = i\left(\frac{Q}{C}\right) \text{ or differentially } P = VC\left(\frac{\mathrm{d}V}{\mathrm{d}t}\right) \tag{8}$$

for a given constant discharge $i = \mathrm{d}Q/\mathrm{d}t = C\,\mathrm{d}V/\mathrm{d}t$ and, for C invariant with potential, $\mathrm{d}V/\mathrm{d}t =$ constant for a given fixed i. In another way, we can write the charge remaining on the capacitor at time t, beyond some initial condition (i) when the charge was Q_i, as

$$Q_t = Q_i - \int i\,\mathrm{d}t \tag{9}$$

The corresponding potential V_t is Q_t/C, i.e.

$$V_t = \left(Q_i - \frac{\int (i\,\mathrm{d}t)}{C}\right) \tag{10}$$

so that the p.d. at time t, after commencement of discharge at i A cm^{-2}, will be

$$P_t = \frac{i(Q_t - \int_0^t t\,\mathrm{d}t)}{C} \tag{11}$$

The initial p.d. (P_i) was iV_i or iQ_i/C (for an initial pootential V_i), so that

$$P_t = iV_i - i\int_0^t \left(\frac{i\,\mathrm{d}t}{C}\right) \tag{12}$$

$$P_t = i\left(\frac{V_i - \int_0^t i\,\mathrm{d}t}{C}\right) \tag{13}$$

which eventually becomes 0 when $\int_0^t (i\,\mathrm{d}t/C) = Q_i/C = V_i$.

Alternatively, a capacitor device could be discharged under conditions of constant power, $iV =$ constant. For such a situation, as charge was being withdrawn and V declining, it would be necessary to arrange instrumentally that i would be increasing in order to maintain the product $iV =$ constant $= k$ say. In fact, the $i = kV^{-1}$, so that the condition

$$\frac{\mathrm{d}i}{\mathrm{d}V} = -kV^{-2} \tag{14}$$

would be required. V (i.e. V_t) at any time t during this constant power discharge would be $V_t = Q_t/C$ in terms of the

charge Q_t remaining at time t into the discharge. Hence

$$\frac{di}{dV} = -\frac{k}{(Q_t/C)^2} \tag{15}$$

that is i must increase as V decreases, which is the obvious basis of this case.

These relations show that p.d. evaluation for a capacitor is not as simple as for an ideal battery. Additionally, as for a battery, the p.d. will decline (at a given degree of charge Q_t held by the capacitor) with increasing discharge rate i when there are *ohmic polarization* losses, as in Eq. (4). This will certainly be the case with porous, high-area capacitor electrodes, especially when less conductive non-aqueous electrolytes are employed as in the case of the higher operating voltage double-layer capacitors.

As with battery systems, the rated p.d. of capacitors will depend on current drain at which the rating is evaluated; it will also depend on the SOC in the capacitor case much more than for most battery systems.

A final difference between capacitor and battery power rating is the relation between p.d. and e.d. for these two types of electrical-energy storage system. Eqs. (5) and (7) show that there is an essentially direct relation between p.d. (iV) and e.d. (QV or $0.5QV$) for a given initial cell voltage since, for both cases, the factor by which the cell voltage is diminished by polarization effects with increasing i or I is, at least theoretically, the same. For capacitors, of course, only the iR or i^2R losses are involved. However, in the case of capacitors, the density of stored energy scales with the *square of the voltage* attained at the end of charge while the p.d. remains linear in that voltage, though for both properties the voltage can be controllably raised (unlike for the case of the thermodynamic voltage of most battery cells) up to, or just below, the electrolyte solution decomposition potential limit (i.e. ca. 1.3 V for aqueous solutions or ca. 3.5–4.0 V for a non-aqueous, aprotic solvent solutions). The above statement implies the important and significant conclusion that the ratio of e.d. to p.d. for a given capacitor is a function of potential on charge, i.e. this ratio *increases* towards completion of charging (or vice versa on discharge) which is not normally the case for ideal battery cells.

6. Modeling calculations for Ragone plots

The following are the bases for calculations of simulated Ragone plots for batteries.

1. An overall polarization equation for electrode potential V as a function of i (including iR and η_a, but excluding concentration polarization) is written (cf. Eq. (6)) as

   $$V = \Delta V_{rev} - iR - (a + b \log i) \tag{16}$$

   Nominal values of $\Delta V_{rev} = 1$ V and $i_0 = 10^{-5}$ A kg^{-1} are taken. The Tafel constant a is $-b \log i_0$.
2. Energy-density, E, is taken as $Q \times V$, where Q is the charge-capacity in MC kg^{-1} (about 10 F), nominally taken as 1 for the purpose of calculations of relative behaviors.
3. Power-density, P, is taken as $i \times V$.
4. V, E, and P are calculated for nominal values of $R = 0.01$, 0.1, 1.0 and 10 Ω, and values of the Tafel parameters a, b, respectively, as 0.6 and 0.120; 0.21 and 0.042; 0.15 and 0.03 V and limitingly as 0 and 0 V (no kinetic polarization). Other values of a, corresponding to various other selected values of ln i_0, could of course, be taken.

The calculations result in a family of 16 log P versus log E curves; the range of i values for each curve was selected such that $V > 0$, i.e. P, $E > 0$, and that the curves covered the range of i values within which the expected maximum in P (from Eq. (5)) would be demonstrated. Note that Eq. (16) predicts (when multiplied by i) an initial increase in P with increasing i when i is sufficiently small that the two polarization terms which diminish V from ΔV_{rev} are negligible but a decrease in P at larger i values; hence a maximum in P arises, as can be shown analytically. However, it is interesting that almost all empirically determined Ragone plots do not exhibit maxima but only a roll-off of P with increasing i and hence diminishing E. This is presumably because, with practical systems, sufficiently high discharge currents were not used in the performance tests to reach and exceed the maximum in P, or alternatively current limitation by diffusion control had set in, as may arise in fuel-cells and some batteries.

Hitherto, only in [12] and later in [13] have fundamental computational treatments been given for Ragone plots for electrochemical capacitors. The following are the bases of the calculations for simulation of Ragone plots for capacitors.

1. An overall polarization equation for electrode potential, V, as a function of i is taken as $V = V_i - iR$.
2. Energy-density, E, is taken as $(1/2)QV = (1/2)CV^2$, where Q is the charge-capacity expressed in MC kg^{-1}, nominally taken here as 1 MC kg^{-1} (about 10 F).
3. Power-density, P, is taken as $i \times V$, as usual.
4. V is a function of SOC (Q/C), as Q declines on discharge.

Fig. 12 illustrates Ragone plots for fully charged capacitors having constant Q (1 MC kg^{-1}), and variable nominal C (2.0, 1.0, 0.5 and 0.1 MF kg^{-1}) values. Each of these cases defines an initial open-circuit potential for a charged capacitor of V_i (0.5, 1, 2, and 10 V). The effect of iR polarization is included in this analysis for nominal R values of $R = 0.1$, 1.0 and 10 mΩ. As discussed by Miller [10], a capacitor is considered effectively discharged when the operating potential falls to $V_i/2$, at which time the capacitor has delivered 75% of its energy into a load resistance. For constant-load discharge, the remaining 25% of capacity can only be recovered over an extended time through the constant

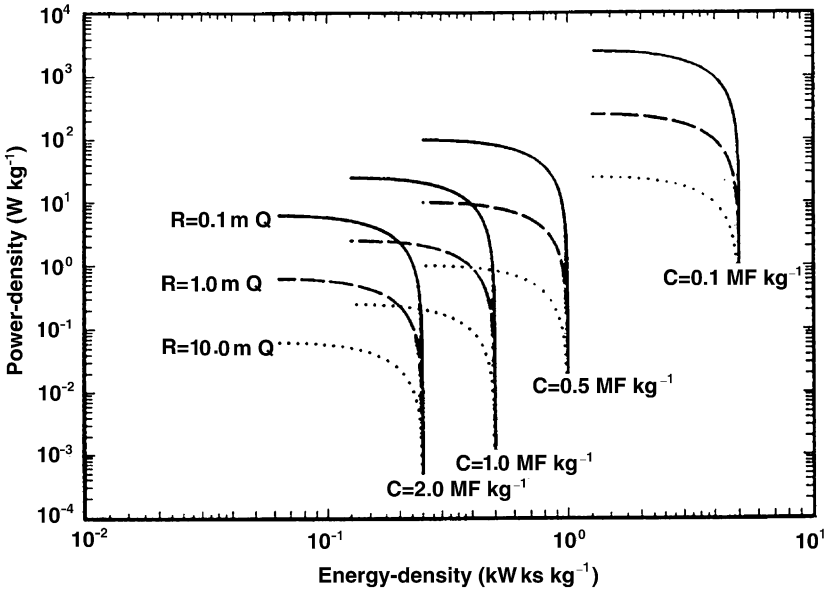

Fig. 12. Calculated Ragone plots for fully charged capacitors having constant $Q = 1$ MC kg^{-1}, variable nominal C (2.0, 1.0, 0.5 and 0.1 MF kg^{-1}) values, and variable ohmic polarization ($R = 0.1$, 1.0, 10.0 mΩ).

resistance load. Thus the curves in Fig. 12 correspond to potentials between V_i and $V_i/2$. Decreasing C, while maintaining Q constant, of course increases the initial operating voltage and thus both the maximum e.d. and p.d. attainable. If the capacitor is discharged past $V_i/2$, both e.d. and p.d. will continue to decrease towards zero. Obviously, decreasing the iR polarization increases the maximum p.d. The maximum e.d. is, however, effectively independent of R, as it always arises as $i \rightarrow 0$.

Fig. 13 shows how the SOC, dependence of e.d. and p.d. values can be calculated as a function of i. Here Q_i (Eq. (9)) is taken as 1 MC kg^{-1}, C as 1 MF kg^{-1}, V_i as 1 V and R as 10 mΩ. Resulting e.d./p.d. relationships were calculated as a function of i for a capacitor holding 56, 36 and 25% of the charge-capacity (on an amp–hour basis) of the fully charged capacitor. Clearly (Fig. 13) both e.d. and p.d. are dependent on the SOC of the capacitor, and the maximum p.d. deliverable by the capacitor decreases as the capacitor is discharged. This is the most significant, but perhaps self-evident, practical characteristic that must be taken into account during system design of battery/capacitor hybrids.

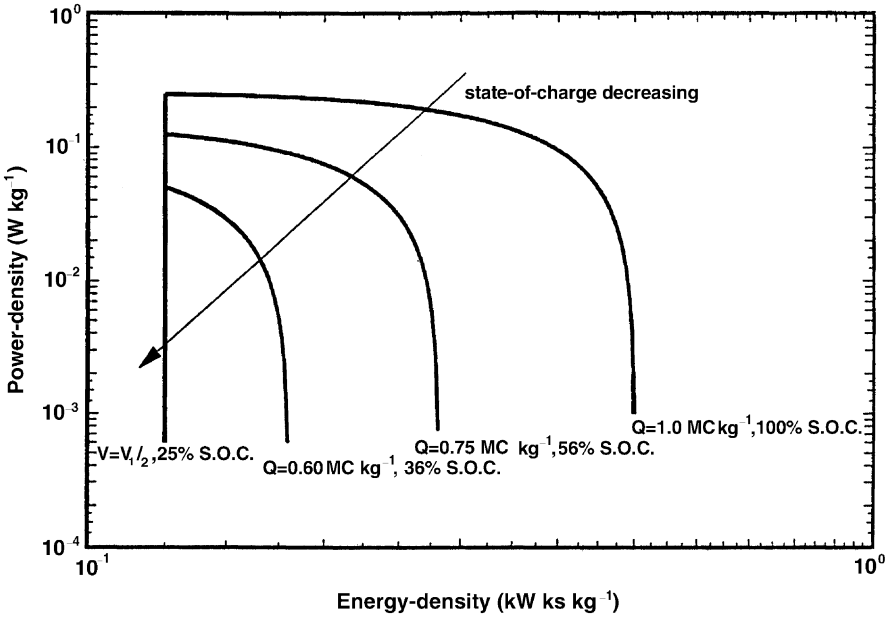

Fig. 13. Calculated Ragone plot showing the SOC dependence of e.d. and p.d. for a capacitor characterized by $Q_i = 1$ MC kg^{-1}, C as 1 MF kg^{-1}, $V_i = 1$ V and $R = 10.0$ mΩ holding 100, 56, 36 and 25% of the charge-capacity (on an amp–hour basis) of the fully charged capacitor.

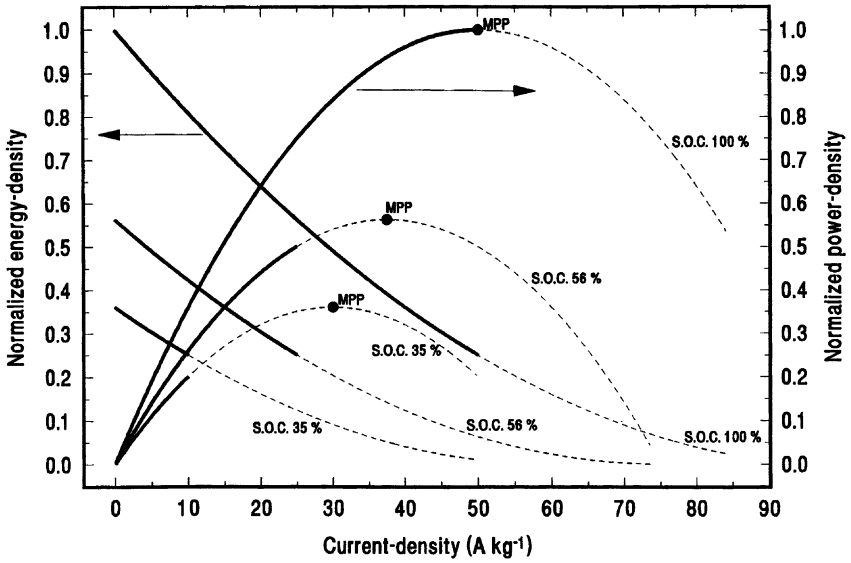

Fig. 14. Normalized e.d. and p.d. vs. i plotted as a function of SOC for a capacitor characterized by $Q_i = 1$ MC kg^{-1}, C as 1 MF kg^{-1}, $V_i = 1$ V and $R = 10.0$ mΩ holding 100, 56 and 36% of the charge-capacity (on an amp–hour basis) of the fully charged capacitor. Solid lines correspond to the e.d. and p.d. up to the "cut-off" voltage for a capacitor discharged down to $V_i/2$; the dashed lines to an e.d. limit of 0.

Fig. 14 illustrates normalized e.d. and p.d. versus i plotted as a function of SOC for the conditions corresponding to Fig. 13. Fig. 14 reinforces the significance of the dependence of both e.d. and p.d. on SOC of the capacitor, and illustrates that there is a maximum power point (MPP) of operation and that it is dependent on SOC. The MPP corresponds to the current-density and device potential at which maximum p.d. may be delivered. In Fig. 14, the dark solid lines correspond to the e.d. and p.d. up to the cut-off voltage for a discharged capacitor of $V_i/2$; the dashed lines to an e.d. limit of 0. As the SOC is decreased, the practical energy limit (viz. 25% of the energy of the fully charged capacitor remaining at the cut-off voltage of $V_i/2$) is reached at progressively lower i's, and clearly this limit is attained at i's smaller than that defined by the MPP. It is, therefore, impossible to operate at the MPP for any SOC other than 100%, illustrating that the choice of the optimum capacitor and its condition of charge (i.e. selection of Q, C, V_i) for a particular application is not a simple problem.

7. Evaluation of electrolyte concentration effects in charge/discharge behavior of a non-aqueous double-layer capacitor

In previous sections of this paper we have considered several complementary aspects of the effects of internal distributed resistance on charge acceptance and resulting limitations of operating p.d. In this section, we show how the charge/discharge behavior of three, specially fabricated, non-aqueous, high-area carbon capacitor cells having sub-optimal concentrations of electrolyte, 1.0, 0.2 and 0.08 M tetrabutylammonium tetrafluoroborate in dry propylene carbonate, depends on the resistivity of the electrolyte and how electrolyte starvation can set in towards high levels of charge for the most dilute electrolyte. This effect was already noticed by Zheng and Jow in an earlier report [14] on another capacitor device. The above sub-optimal concentrations (below 1.0 M) were selected to enhance (and hence to better evaluate) the consequences of distributed internal resistance upon charging and discharging under CV and application of dc.

It will be noted that real capacitor devices are fabricated with maximum concentrations of electrolytes, or with maximum conductivities of such solutions in order to minimize power losses of the type discussed in this paper. Indeed, impressively low resistivities are achieved in current, state-of-the-art systems but with non-aqueous capacitor embodiments internal resistances are unavoidably higher than with aqueous solution devices and the results given here are hence more relevant to behavior of the former type; however, in the present work, electrolyte concentrations, significantly smaller than those optimally employed in practical device construction, have been used specially to be able to evaluate internal resistance distribution effects, leading to power limitations, more accurately and systematically than would otherwise be possible using empirically chosen, commercially available devices.

Fig. 15a–c shows cyclic voltammograms recorded at 1, 5, 10 and 20 mV s^{-1} for the three above electrolyte concentrations over a 3 V range in capacitor modules fabricated for us by Redox Engineering Inc. The response behavior is expressed as reduced current, I/s, corresponding to capacitance (Eq. (1)), with increasing dilution of the electrolyte (i.e. increasing specific resistivity). It is seen how the voltammograms are progressively more distorted from the ideal rectangular profiles expected (for constant C) as s increases and as the electrolyte concentration is decreased. Interestingly, in Fig. 15c, beyond about 1.5 V, the RC response

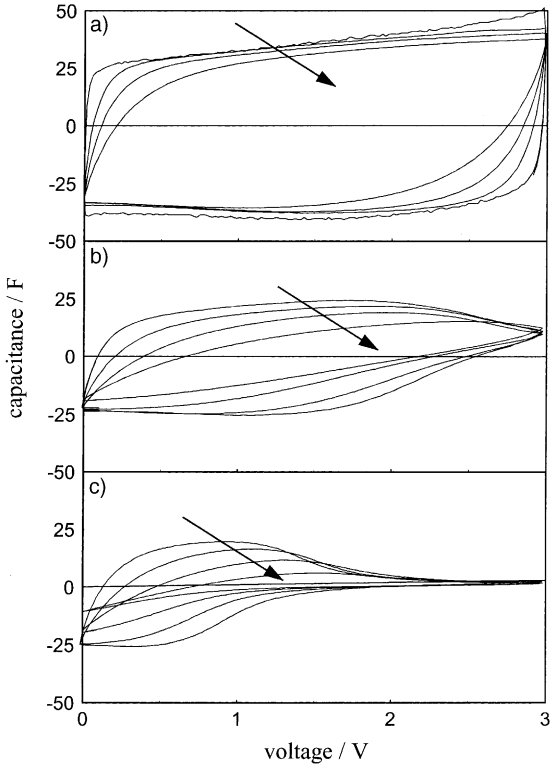

Fig. 15. Cyclic voltammograms for non-aqueous carbon capacitor cells expressed as capacitance (I/s) vs potential at (a) 1, 5, 10 and 20 mV s^{-1} in 1.0 M tetrabutylammonium tetrafluoroborate in dry propylene carbonate; (b) 5, 10, 20 and 40 mV s^{-1} in 0.2 M tetrabutylammonium tetrafluoroborate in dry propylene carbonate; (c) 5, 10, 20 and 40 mV s^{-1} in 0.08 M tetrabutylammonium tetrafluoroborate in dry propylene carbonate; arrows indicate direction of increasing sweep-rate, s.

declines towards zero as the charging voltage approaches 3.0 V for the case of the 0.08 M electrolyte. This is due to a combination of the usual distributed resistance effect down pores and especially to free-electrolyte starvation since, for the amount of electrolyte present in that solution, almost all its ions become adsorbed at the high-area interface enhancing the internal resistance effect towards full SOC.

Corresponding effects arise under dc charge/discharge conditions for increasing discharge/recharge current-densities. Increasing sweep-rate (i.e. corresponding to charging at higher power-densities) causes diminution of charge admission, the effect being larger at lower concentrations (larger resistivities). These effects are also manifested in corresponding Ragone plots. As expected, the deliverable powers and energies become strongly attenuated with increasing dilution of the electrolyte.

While design of electrochemical capacitors calls for minimum solution resistivities, the above results give clear and quantitative demonstrations of the effects of increasing distributed resistance and also the effects of electrolyte starvation observable towards full SOC.

Acknowledgements

Grateful acknowledgment is made to the Natural Sciences and Engineering Research Council of Canada for support of this work on a Strategic Grant. Thanks are due to Dr. N. Marincic of Redox Engineering Inc. (Winchester, MA) for preparing the non-aqueous solution capacitor modules.

References

[1] S. Trasatti, G. Buzzanca, J. Appl. Electrochem. 4 (1974) 57.
[2] B.E. Conway, V.I. Birss, H.A. Kozlowska, J. Wojtowicz, J. Power Sources 66 (1997) 1.
[3] B.E. Conway, J. Electrochem. Soc. 138 (1991) 1539.
[4] B.E. Conway, Electrochemical Supercapacitors: Scientific Fundamentals and Technological Applications, Plenum Press, New York, 1999.
[5] R. de Levie, Electrochim. Acta 8 (1963) 751.
[6] H. Keiser, K.D. Beccu, M.A. Gutjar, Electrochim. Acta 21 (1976) 539.
[7] R. de Levie, Electrochim. Acta 9 (1964) 1231.
[8] D.V. Ragone, in: Proceedings of the Automotive Engineers Conference on Review of Battery Systems for Electrically Powered Vehicles, Society of Automotive Engineers, Warrendale, PA, 1968.
[9] B.E. Conway, in: S. Wolsky, N. Marincic (Eds.), Proceedings of the 7th Symposium on Double-Layer Capacitors and Similar Energy Storage Devices, Florida Educational Seminars Inc., Boca Raton, FL, 1997.
[10] J. Miller, in: S. Wolsky, N. Marincic (Eds.), Proceedings of the 4th International Seminar on Electrochemical Capacitors and Similar Energy Storage Devices, Florida Educational Inc., Boca Raton, FL, 1994.
[11] B.E. Conway, E. Gileadi, Trans. Faraday Soc. 58 (1962) 2493.
[12] W.G. Pell, B.E. Conway, J. Power Sources 63 (1996) 255.
[13] D. Dunn, J. Newman, J. Electrochem. Soc. 147 (2000) 820.
[14] J.P. Zheng, T.R. Jow, J. Electrochem. Soc. 144 (1997) 2417.